npj | climate and atmospheric science

Article

Published in partnership with CECCR at King Abdulaziz University

https://doi.org/10.1038/s41612-025-01143-4

# Energetic processes underlying the interannual variability of South Asian summer monsoon



Tong Lu[1,2,3,4], Kaiming Hu[1,3] ✉, Gang Huang[1,2,4] ✉, Sang-Wook Yeh[5] & Ya Wang[1]

The South Asian summer monsoon (SASM) interannual variability significantly impacts regional climates, with its first mode featuring a lower-level anomalous anticyclone over the northern Bay of Bengal (BOB) and the second mode displaying an anomalous anticyclone over central-northern India. Here, we diagnose the energy budget of these two SASM modes. Barotropic energy conversion supplies eddy kinetic energy (EKE) to the first mode from lower-level climatological confluent westerlies downstream of the Somali Jet and over the BOB–western North Pacific. In contrast, the second mode derives EKE from the subtropical westerly confluence induced by Tibetan Plateau topography. Baroclinic energy conversion, extracting eddy available potential energy (EAPE) from the mean thermal structure, sustains the second mode while dampening the first. Convective heating generates EAPE for both modes, acting as feedback. Further analyses suggest these modes likely stem from internal dynamics. Our findings highlight the importance of internal energetic processes in SASM modulation.

Characterized by strong, warm and moist flow, the South Asian summer monsoon (SASM) profoundly influences local agriculture, hydrology, and economic development, thereby impacting billions of livelihoods[1–3]. As a vital component of the global monsoon system, SASM can impact the remote climate, especially over East Asia[4–8], through teleconnection wave trains, triggering extreme events such as Yangtze River heatwaves[9] and northwest Pacific marine heatwaves[10]. Its associated diabatic heating also modulates Arctic Sea ice variability, highlighting its role in tropical-polar interactions[11]. Moreover, SASM is critical in shaping the accuracy among the coupled model simulations for the circumglobal teleconnection pattern[12]. Consequently, investigating the dynamic origins of SASM is essential for regional climate prediction.

The SASM exhibits significant interannual variability, with two dominant modes according to previous studies[13–16]. One mode is characterized by a northwest-southeast elongated tripolar rainfall pattern in South Asia with an anomalous anticyclone over the northern Bay of Bengal (BOB), while the other features the suppressed rainfall in India associated with a local anticyclonic anomaly (Fig. 1). These two leading modes are closely related to the El Niño/Southern Oscillation (ENSO) cycle. During the ENSO decaying phase, the westward Rossby wave generated by suppressed convection over the western North Pacific (WNP), together with the eastward Kelvin wave induced by warm sea surface temperature (SST) anomalies in the tropical Indian Ocean (TIO), jointly influence the South Asian tripolar precipitation mode[17,18]. During the ENSO developing phase, the Indian rainfall suppression mode is influenced by the westward Rossby wave triggered by the suppressed convection over the Maritime Continent associated with Walker circulation[19,20].

Apart from the ENSO, other external atmospheric forcings also modulate the SASM interannual variability. Regarding local SSTs, the Indian Ocean Dipole mode can affect SASM by modulating cross-equatorial flow[21], while SST anomalies in the South Indian Ocean alter the meridional SST gradient, thereby modulating the local Hadley circulation and further impacting SASM[22,23]. For remote SSTs, the equatorial Atlantic SST zonal mode[24] and North Atlantic SST anomalies[25] can affect SASM rainfall via Kelvin and Rossby wave responses, respectively. In addition to SST effects, the Tibetan Plateau (TP) can modulate the SASM through thermal and mechanical effects[26]. The strong surface sensible heat over the TP during spring can regulate the establishment of the Asian summer monsoon[27,28], while the TP topography is a key factor determining the SASM to extend across the entire Indian subcontinent[29,30]. Moreover, positive Eurasian snow

[1]State Key Laboratory of Earth System Numerical Modeling and Application, Institute of Atmospheric Physics, Chinese Academy of Sciences, Beijing, China. [2]Laboratory for Regional Oceanography and Numerical Modeling, Qingdao National Laboratory for Marine Science and Technology, Qingdao, China. [3]Center for Monsoon System Research, Institute of Atmospheric Physics, Chinese Academy of Sciences, Beijing, China. [4]University of Chinese Academy of Sciences, Beijing, China. [5]Department of Marine Science and Convergence Engineering, Hanyang University, Ansan, South Korea. ✉e-mail: hkm@mail.iap.ac.cn; hg@mail.iap.ac.cn

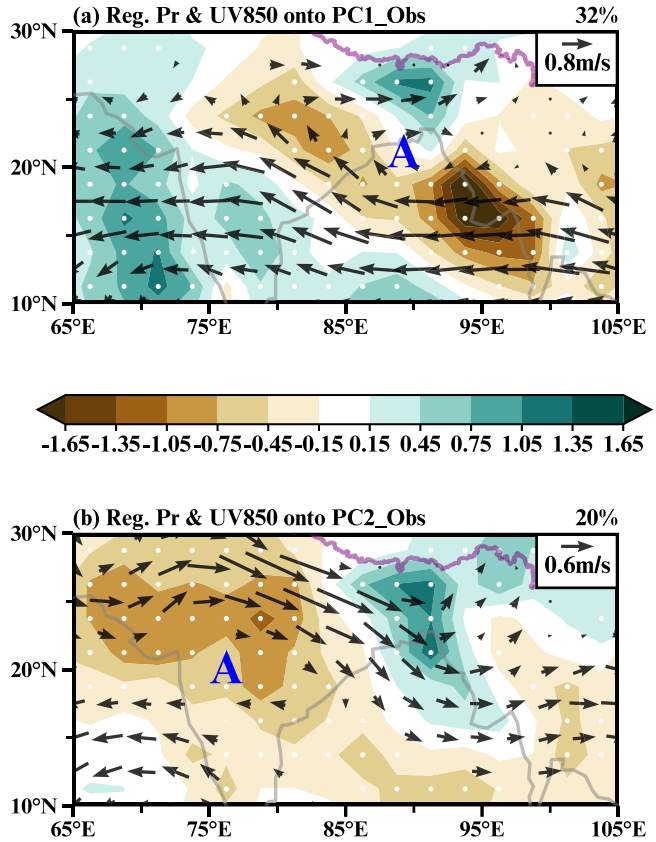


**Fig. 1 | Circulation characteristics of the two leading modes for SASM interannual variability in observations.** Spatial patterns of the (**a**) first and (**b**) second MV-EOF modes for the June-August (JJA) precipitation from the Climate Research Unit (CRU) dataset and 850 hPa zonal wind over South Asia (10°–30°N, 65°–105°E) during 1979–2022. To clearly show the associated physical processes, the rainfall (shading; mm day$^{-1}$) from the Global Precipitation Climatology Project (GPCP) dataset and 850 hPa horizontal winds (vectors; m s$^{-1}$) are regressed onto the observed principal components (PCs_Obs), respectively. Stippling areas indicate regression coefficients of precipitation passing the 90% confidence level. Only wind regression coefficients exceeding the 90% confidence level are shown. The blue letters A denote the centers of the anomalous anticyclones. The purple contour indicates the extent of the TP, and the same applies to other figures.

cover anomalies during winter and spring tend to be followed by a decreased SASM rainfall[31–33].

These atmospheric external forcings provide a physical basis for SASM prediction[34,35]. Beyond them, SASM interannual variability could also be modulated by the atmospheric internal dynamic processes unrelated to the variability of SSTs and boundary conditions[36,37]. In boreal summer, the Indo-Western Pacific is characterized by lower-level climatological confluent flow between monsoon westerlies and easterly trades, accompanied by the pronounced land-sea thermal contrast. Previous studies have shown that local atmospheric patterns can extract eddy energy from this background state. Hu et al.[38] found that the WNP anomalous anticyclone (WNPAC), playing an important role in modulating the SASM variability[18], can extract eddy kinetic energy (EKE) from climatological mean flow via barotropic energy conversion, which helps anchor its location. Similarly, Kosaka and Nakamura[39] discovered that the tilted vertical structure of the Pacific–Japan (PJ) pattern, which can influence the SASM[20,40], facilitates the extraction of eddy available potential energy (EAPE) from the climatological thermal structure by baroclinic energy conversion, sustaining the PJ pattern. These results highlight the crucial role of eddy energy conversion from the mean state across the Indo-Western Pacific in local atmospheric modes. However, the contribution of such a mean state to the interannual variations of SASM remains largely unclear.

Motivated by this conundrum, the present study aims to investigate how the mean state influences the two dominant modes of SASM interannual variability from the energetic perspective. Based on the multivariate empirical orthogonal function analysis (MV-EOF)[41], the observed two leading modes of SASM interannual variability and associated circulation features are identified first. By doing so, the energy budget processes between the Indo-Western Pacific background state and the two leading SASM anomalies are further investigated through energy diagnostic equations. At last, analyses based on ENSO-independent circulations and different model experiments are conducted to confirm whether these leading SASM modes originate from internal atmospheric dynamics.

## Results

### Leading modes of SASM interannual variability in observations

Given that precipitation and zonal wind are widely used to characterize the Asian summer monsoon[42–44], the two leading modes of SASM are obtained through the MV-EOF[41] on the interannual component of 850 hPa zonal wind and terrestrial precipitation over South Asia (10°–30°N, 65°–105°E)[15] from 1979 to 2022 (see "Methods"). Figure 1 shows the spatial patterns for the two dominant modes of SASM interannual variability, which explain 32 and 20% of the total variance, respectively, and are statistically independent from other modes[45].

Consistent with previous studies[16], the positive phase of the first MV-EOF mode exhibits a nearly northwest-southeast elongated tripolar precipitation pattern. It features negative anomalies along northeastern India to northeastern BOB, flanked by two positive centers—one in the northern BOB and the other extending from the eastern Arabian Sea to the southern BOB (Fig. 1a). This precipitation pattern is accompanied by significant lower-level anomalous easterlies around 15°N spanning from the tropical western Pacific to the Arabian Sea and an anomalous anticyclone over northern BOB, accompanied by a significantly enhanced WNPAC (Supplementary Fig. S1). These features indicate a westward extension of the WNPAC[18] and a weakened Indian monsoon trough (IMT)[15]. The positive phase of the second MV-EOF mode is characterized by a positive precipitation center in the northern BOB and negative anomalies across the rest of South Asia, particularly in central-northern India (Fig. 1b). It is accompanied by a lower-level anomalous anticyclone centered over central-northern India, with prominent westerly anomalies to its north. The corresponding negative phases are depicted by circulation and precipitation anomaly patterns similar to those discussed above, but with reversed polarity. Therefore, for conciseness, this study focuses on the positive phases of the two leading SASM modes.

It is noted that both the first and second SASM modes are characterized by zonally elongated circulation anomalies ($u'^2 > v'^2$) at 850 hPa. As demonstrated by Simmons et al.[46], such a structure of perturbations can readily extract EKE from a background zonal confluent flow, thereby sustaining its development[38,39,47]. Motivated by this, we will analyze the energy conversion processes that effectively support the first two SASM modes in the following section to understand energy sources sustaining SASM interannual variability.

### Energy conversion between the mean field and perturbations

Based on Eq. (1), the barotropic energy conversion ($CK$) associated with two leading SASM modes from the background mean flow to perturbations is estimated (see "Methods"). During the boreal summer, South Asia is dominated by significant climatological monsoon westerlies at lower levels. To the west of South Asia, which lies downstream of the Somali Jet[48], the climatological westerlies exhibit a confluent pattern, resulting in a pronounced negative $\frac{\partial \bar{u}}{\partial x}$. On the eastern coastline of India, monsoon westerlies flow through the IMT, subsequently deflecting slightly northward and interacting with the easterly trades from the central Pacific over the WNP. This forms a broad zonal confluent zone spanning the BOB-WNP region[38] and can be depicted by negative $\frac{\partial \bar{u}}{\partial x}$ at around 15°N. Additionally, when subtropical westerlies from the Arabian Peninsula merge with the Somali Jet and extend across South Asia[49], the dynamic influence of the TP topography

induces significant zonal wind confluence over northeastern India. These circulation features above at 850 hPa characterize South Asia (10°–30°N, 65°–105°E) as a background zonal confluent zone. Based on Eq. (1), zonally elongated anomalies associated with two SASM modes ($u'^2 > v'^2$; Fig. 1) can readily induce positive *CK* in such confluent zone ($\frac{\partial \bar{u}}{\partial x} < 0$; Fig. 2)[46], which will be discussed in detail next.

Figure 3 further estimates the *CK* associated with the two SASM modes superimposed on the background zonal confluent flow (see "Methods"). For the first SASM mode, significantly positive *CK* lies on the background zonal confluent zone ($\frac{\partial \bar{u}}{\partial x} < 0$; Fig. 2) downstream of the Somali Jet and over the BOB–WNP at around 15°N (Fig. 3a). The $CK_x$, representing energy conversion from the background confluent flow to perturbations, plays a dominant role in inducing lower-level *CK* (Fig. 3b) due to the zonally elongated anomalous easterlies of the first SASM mode ($u'^2 > v'^2$; Fig. 1a and Supplementary Fig. S1a)[50]. It can readily extract EKE through conversion from mean kinetic energy (MKE) and sustain the first SASM mode.

The negative *CK* over northeastern India is induced by energy conversion from perturbations to the mean horizontal wind shear (negative $CK_y$; Fig. 3c), corresponding to the local negative $\frac{\partial \bar{u}}{\partial y}$ induced by the climatological IMT (Fig. 2). This structure is unfavorable for anomalous southeasterlies at 20°N ($u'v' < 0$; Fig. 1a) to extract EKE from the local mean state, thereby damping the first mode. Nevertheless, the area-mean *CK* at 850 hPa over South Asia is $0.47 \times 10^{-6}$ m$^{-2}$s$^{-3}$, suggesting that *CK* overall contributes to the development of the first SASM mode.

To measure the efficiency of *CK* at 850 hPa in the maintenance of the first SASM mode, we evaluate the time scale ($\tau_{CK}$; see "Methods") to denote how long it takes for the local EKE to be fully replenished through *CK*[39]. For the first SASM mode, the $\tau_{CK}$ is 6.9 days, which is close to the friction damping time scale at lower levels[51], suggesting that *CK* is efficient enough to maintain the first SASM anomalies[38].

For the second SASM mode, the maximum positive *CK* is located in the background zonal confluent zone ($\frac{\partial \bar{u}}{\partial x} < 0$; Fig. 2) over northeastern India (Fig. 3d), attributed to local $CK_x$ (Fig. 3e). It denotes that local zonally elongated anomalous northwesterly of the second SASM mode ($u'^2 > v'^2$; Fig. 1b) can easily gain EKE from the subtropical westerly confluence due to the TP topography, supplying their development. In contrast, $CK_y$ is negative in the same region (Fig. 3f), which is unfavorable for anomalous northwesterly ($u'v' < 0$; Fig. 1b) to extract EKE from the background of the negative $\frac{\partial \bar{u}}{\partial y}$ (Fig. 2). Overall, the stronger positive $CK_x$ can offset the damping effect of $CK_y$, generating local EKE through conversion from MKE. The positive *CK* facilitates the development of anticyclonic anomalies over central-northern India for the second SASM mode. The corresponding area-averaged *CK* at 850-hPa over South Asia is $0.28 \times 10^{-6}$ m$^{-2}$s$^{-3}$ and the $\tau_{CK}$ is 4.0 days, indicating that *CK* is adequate to maintain the second SASM mode, offsetting damping processes at lower levels.

In addition to EKE, EAPE is another energy source influencing the position and structure of key climate systems from the tropics to the subtropics[39]. Based on Eq. (3), the baroclinic energy conversion (*CP*) from mean available potential energy (MAPE) to EAPE is diagnosed (see "Methods"). Figure 4 displays the vertically integrated *CP* from 1000 to 200 hPa associated with the two SASM modes, along with the climatological temperature vertically averaged from 300 to 200 hPa and 850 to 700 hPa, respectively. In summer, at upper levels, climatological temperature shows a warm center over the western TP, with positive and negative $\frac{\partial \bar{T}}{\partial x}$ over northwestern India and southeastern TP, respectively, and a pronounced positive $\frac{\partial \bar{T}}{\partial y}$ across South Asia (Fig. 4a). At lower levels, the warm center is located over the Arabian Peninsula, accompanied by a notable negative $\frac{\partial \bar{T}}{\partial x}$

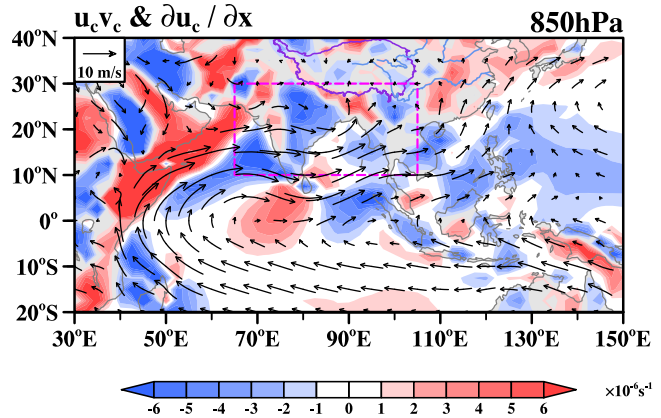


**Fig. 2 | Climatological lower-level circulations across the Indo-Western Pacific in boreal summer.** JJA climatological horizontal wind (vectors; m s$^{-1}$) and the zonal gradient of climatological zonal wind (shading; s$^{-1}$) at 850 hPa from 1979 to 2022. The pink dashed box indicates the South Asian region (10°–30°N, 65°–105°E).

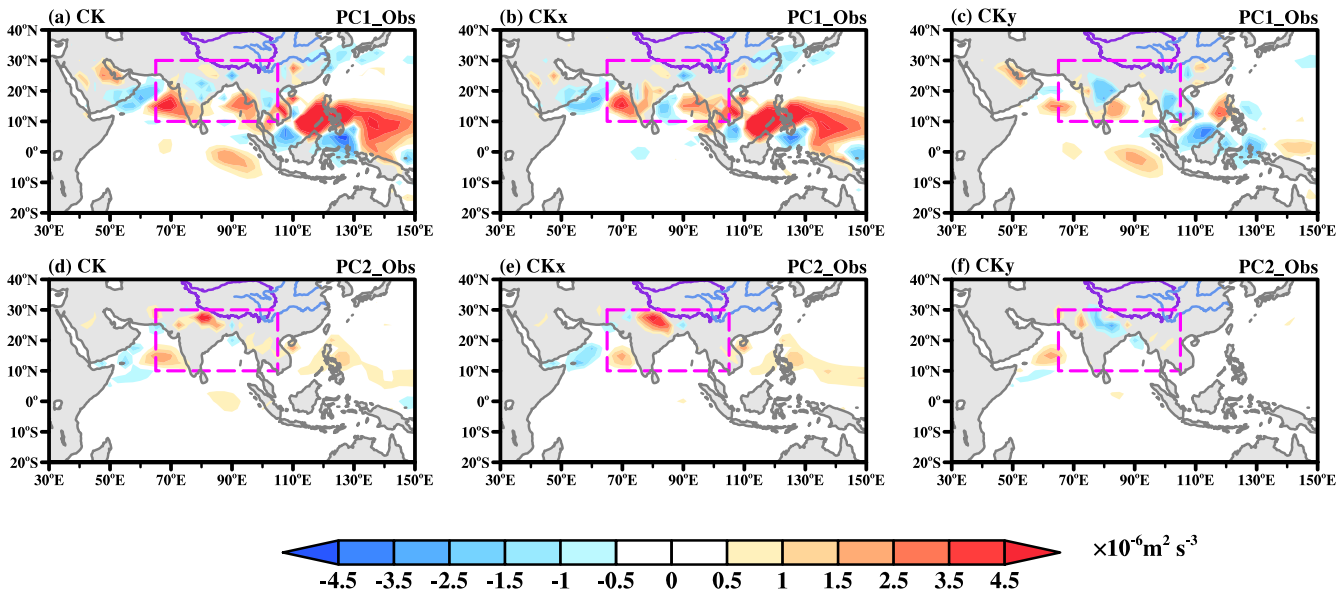


**Fig. 3 | Barotropic energy conversion for the two leading SASM modes superimposed on the mean flow. a** *CK*, (**b**) $CK_x$, and (**c**) $CK_y$ in Eq. (1) at 850 hPa (shading; $\times 10^{-6}$ m$^2$s$^{-3}$), calculated from perturbations ($u'$, $v'$) regressed onto PC1_Obs. **d**–**f** Are the same as (**a**–**c**), but for PC2_Obs. The pink dashed box indicates the South Asian region (10°–30°N, 65°–105°E).

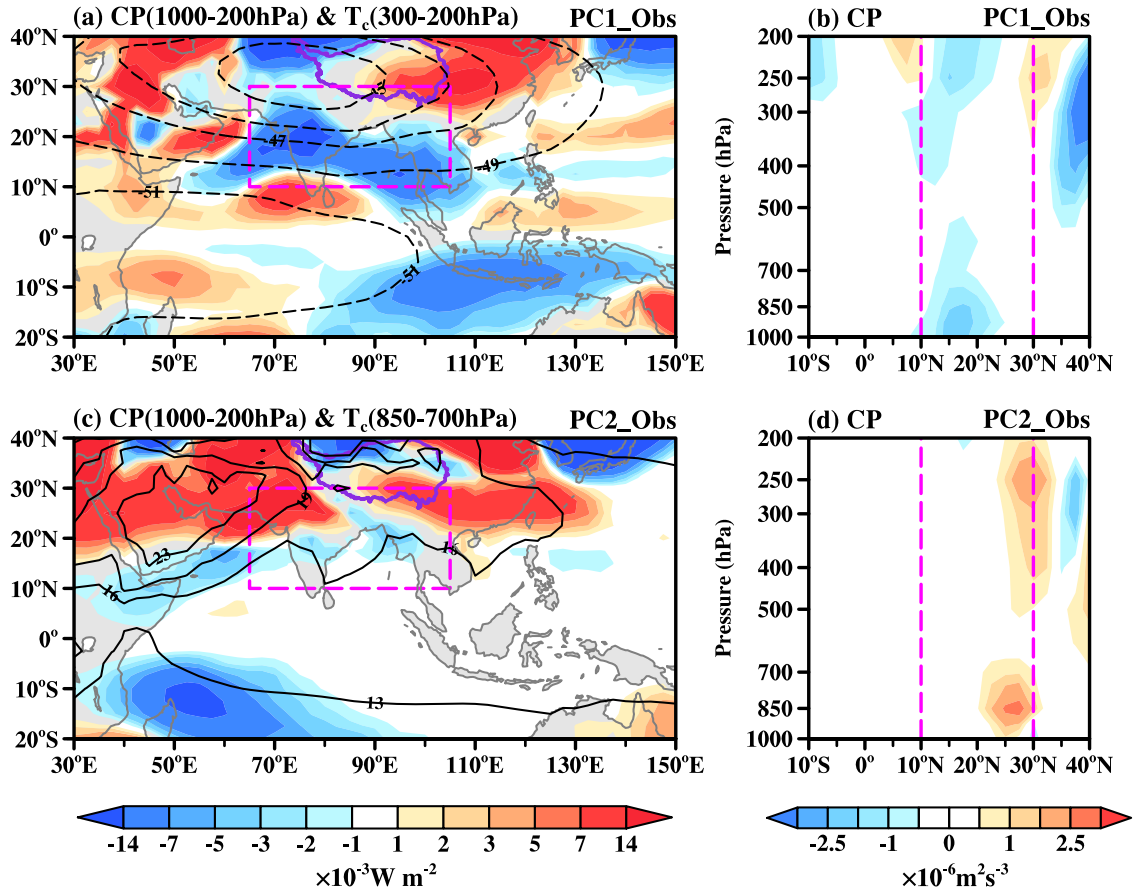


**Fig. 4 | Baroclinic energy conversion for the two leading SASM modes superimposed on the mean thermal structure. a** Vertically integrated *CP* in Eq. (3) from 1000 to 200 hPa (shading; $\times 10^{-3}$ W m$^{-2}$), calculated from perturbations ($u'$, $v'$, $T'$) regressed onto PC1_Obs. **b** Vertical profiles of *CP* zonally averaged over 65°–105°E (shading; $\times 10^{-6}$ m$^2$s$^{-3}$) for PC1_Obs. **c**–**d** Are the same as (**a**, **b**). but for PC2_Obs. Contours in (**a**) and (**c**) represent summer climatological temperature (°C) vertically averaged from 300 to 200 hPa and 850 to 700 hPa, respectively. The pink dashed box in (**a**) and (**c**) indicates the South Asian region (10°–30°N, 65°–105°E). The pink dashed lines in (**b**) and (**d**) indicate the latitudinal range of South Asia (10°–30°N).

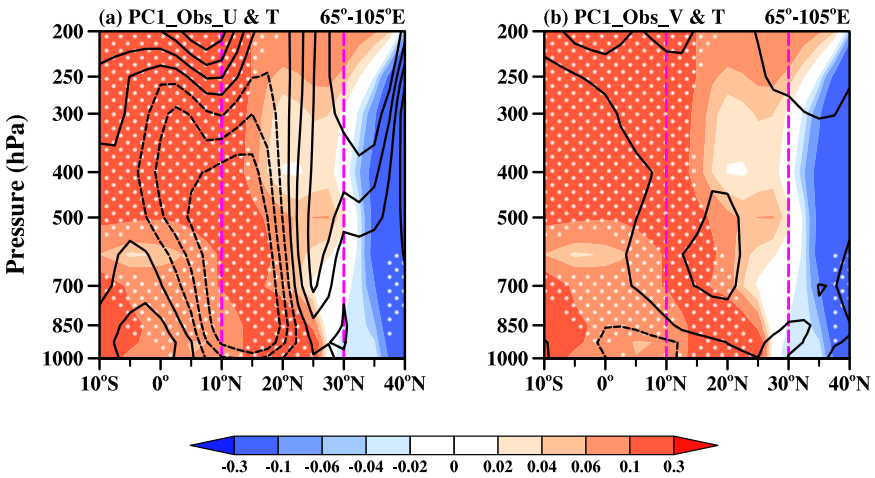


**Fig. 5 | Vertical structure of the thermal and horizontal wind anomalies for the first SASM mode.** Vertical profiles of anomalous temperature (shading; K) and (**a**) zonal and (**b**) meridional winds (contour; m s$^{-1}$) regressed onto PC1_Obs and zonally averaged over 65°–105°E. The pink dashed lines indicate the latitudinal range of South Asia (10°–30°N). Stippling areas indicate regression coefficients of temperature passing the 90% confidence level. The contour interval is 0.2 m s$^{-1}$ (0, ±0.2, ±0.4, ±0.6).

over northwestern India (Fig. 4c). Such a mean thermal structure may interact with the eddy heat fluxes ($u'T'$ and $v'T'$), leading to conversion between MAPE and EAPE[39,47].

For the first SASM mode, the negative *CP* dominates South Asia, with centers at both lower and higher levels (Fig. 4a, b). We further decompose *CP* into $CP_x$ and $CP_y$ (see "Methods" and Supplementary Figs. S2 and S3). The pronounced negative $CP_y$ over entire South Asia at higher levels makes the dominant contribution to the total negative *CP* (Supplementary Figs. S2c and S3c), resulting from the upper-level positive $\frac{\partial \bar{T}}{\partial y}$ (Fig. 4a) enhanced by the northward eddy heat flux from offshore to inland ($v'T' > 0$; Fig. 5b). The lower-level negative *CP* stems from $CP_x$ (Supplementary Figs. S2b and S3b), driven by a consistent positive $\frac{\partial \bar{v}}{\partial p}$ and negative $u'T'$ over South Asia (Fig. 5a and Supplementary Fig. S4). They jointly increase local MAPE while consuming EAPE, damping the first SASM anomalies.

In contrast to the first SASM mode, *CP* associated with the second mode is significantly positive over northwestern India and southeastern TP,

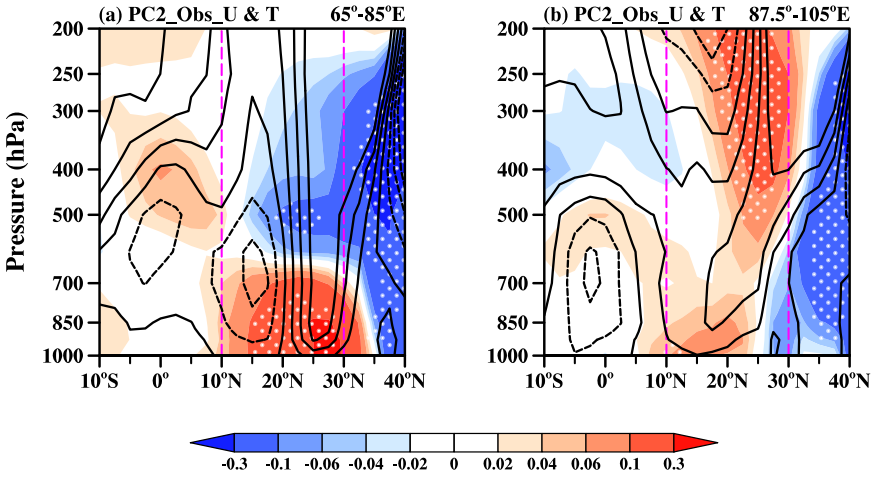


**Fig. 6 | Vertical structure of the thermal and zonal wind anomalies for the second SASM mode.** Vertical profiles of anomalous temperature (shading; K) and zonal wind (contour; m $s^{-1}$) regressed onto PC2_Obs and zonally averaged over (**a**) 65°–85°E and (**b**) 87.5°–105°E, respectively. The pink dashed lines indicate the latitudinal range of South Asia (10°–30°N). Stippling areas indicate regression coefficients of temperature passing the 90% confidence level. The contour interval is 0.2 m $s^{-1}$ (0, ±0.2, ±0.4, ±0.6).

with centers at both lower and higher levels between 20°N and 30°N (Fig. 4c, d). This distribution of *CP* is primarily attributed to the $CP_x$ (Supplementary Figs. S2e and S3e). Given the dipole zonal temperature anomalies between 20°N and 30°N over South Asia (figure not shown), we calculate the zonal average $u'$ and $T'$ over 65°–85°E and 87.5°–105°E, respectively (Fig. 6). Over 65°–85°E, eastward eddy heat flux ($u'T' > 0$; Fig. 6a) at lower levels between 20°N and 30°N tends to weaken the negative $\frac{\partial \bar{T}}{\partial x}$ over northwestern India (Fig. 4c). At higher levels, westward eddy heat flux ($u'T' < 0$; Fig. 6a) acts to reduce the local positive $\frac{\partial \bar{T}}{\partial x}$ in the same region (Fig. 4a). Similarly, over 87.5°–105°E, positive $u'T'$ at higher levels around 30°N (Fig. 6b) can weaken the negative $\frac{\partial \bar{T}}{\partial x}$ over southeastern TP (Fig. 4a). Thus, they jointly enhance EAPE through conversion from the mean thermal structure, supplying the second SASM anomalies. According to Lau and Lau[52], the EAPE generated by *CP* can further be converted to EKE, aiding the anomalous circulations directly.

Similar to barotropic energy conversion, we estimate the time scale of effective *CP* in replenishing the local EAPE associated with the first two SASM modes ($\tau_{CP}$; see "Methods"). Related to the first SASM mode, the $\tau_{CP}$ is -2.4 days, while that is 2.7 days for the second mode. It means that the *CP* can dampen the first SASM mode but significantly sustain the second mode. For the second SASM mode, the positive *CP* over northwestern India and southeastern TP at higher levels indicates its complexity, which may be influenced by mid-latitude baroclinic atmospheric processes[4,15].

Based on the analysis above, both barotropic and baroclinic energy conversions act as potential processes for extracting eddy energy from the climatological mean state. In addition, as the feedback to the circulations, the energy conversion from convective latent heating also serves as a key source of EAPE (*CQ*; see "Methods"), facilitating the development of atmospheric modes[39,47,52]. According to Eq. (5), positive *CQ* indicates that heating (cooling) intensifies warm (cold) anomalies, leading to the generation of EAPE from anomalous convective heating. As demonstrated by Lau and Lau[52], the EAPE generated by *CQ* can be further converted into EKE through the EAPE balance, thereby directly supporting anomalous circulation. The vertically integrated *CQ* from 1000 to 200 hPa is shown in Fig. 7.

For the first SASM mode, *CQ* is pronounced positive in eastern TIO attributed to the local diabatic heating and warm anomalies ($T'Q_1' > 0$; Fig. 8). In South Asia, *CQ* exhibits prominently positive anomalies over the eastern Arabian Sea and north of the BOB above 500 hPa, while negative anomalies appear in the region between them below 700 hPa (Fig. 7a, b). Accompanied by warm anomalies over South Asia (Fig. 8), diabatic heating over the eastern Arabian Sea and north of the BOB intensifies the warm temperature perturbations ($T'Q_1' > 0$), thereby increasing local EAPE, while diabatic cooling in between suppresses the warm perturbations ($T'Q_1' < 0$), acting to reduce local EAPE. The time scale for *CQ* to replenish the local EAPE is further quantified ($\tau_{CQ}$; see "Methods"). Although *CQ* in different regions can offset each other, the $\tau_{CQ}$ across South Asia is 2.2 days for the first SASM mode. It suggests that the anomalous convective heating can contribute effectively to the amplification of the first SASM anomalies.

For the second SASM mode, *CQ* is positive over northwestern India and north of the BOB, accompanied by a pronounced positive center near 30°N above 500 hPa. The modestly negative *CQ* is observed over the northeastern India and northwestern Indo-China Peninsula below 700 hPa (Fig. 7c, d). The associated vertical profiles of anomalous diabatic heating and temperature are illustrated in Fig. 9, with the same two subregions as Fig. 6. Within 65°–85°E (87.5°–105° E), diabatic cooling (heating) amplifies cold (warm) perturbations over northwestern India (north of the BOB) at mid-to-upper troposphere ($T'Q_1' > 0$). These processes together generate EAPE to supply the second SASM mode. Conversely, the diabatic cooling over the 65°–85°E may suppress the local warm temperature perturbations from 850 to 700 hPa, acting to dampen the second mode. The corresponding $\tau_{CQ}$ is 2.5 days averaged in South Asia, indicating that anomalous convective heating has a net contribution to the maintenance of the second SASM mode. The above diagnosis aligns with the findings of Lau and Lau[52], indicating that diabatic heating due to cumulus convection at mid-to-upper levels serves as a key source of EAPE for Indo-Western Pacific perturbations.

### Leading modes of SASM interannual variability independent of external forcings

Previous studies suggest that some atmospheric patterns, such as the Pacific-North American (PNA) teleconnection, PJ pattern, and WNPAC[38,39,46], may be internal modes sustained by extracting eddy energy from the mean state, thereby persisting even in the absence of external forcing. Based on the energy analysis above, the mean state across South Asia contributes to the development of two dominant SASM anomalies. Therefore, this section investigates whether the two leading SASM modes can exist without external forcings, namely SSTs and boundary conditions.

We first examine the SASM interannual variability independent of ENSO, the critical external forcing. A linear regression approach is employed to simultaneously remove the linear impact of ENSO in the preceding winter and the concurrent summer on SASM (see "Methods")[53,54]. The two leading modes of SASM interannual variability without ENSO are further captured using a similar MV-EOF analysis, passing the North's test. The explained variance of the first and second SASM modes decreases to 28 and 19%, respectively. As shown in Fig. 10a, b, the key circulation characteristics for the first two SASM modes remain remarkable after removing ENSO's linear effect.

For the positive phase of the first mode, the northwest-southeast elongated tripolar precipitation pattern exhibits weakened negative anomalies in northeastern India and reduced positive anomalies in the northern BOB. Similarly, lower-level westerly anomalies along the north flank of the anomalous anticyclone over northern BOB are also reduced,

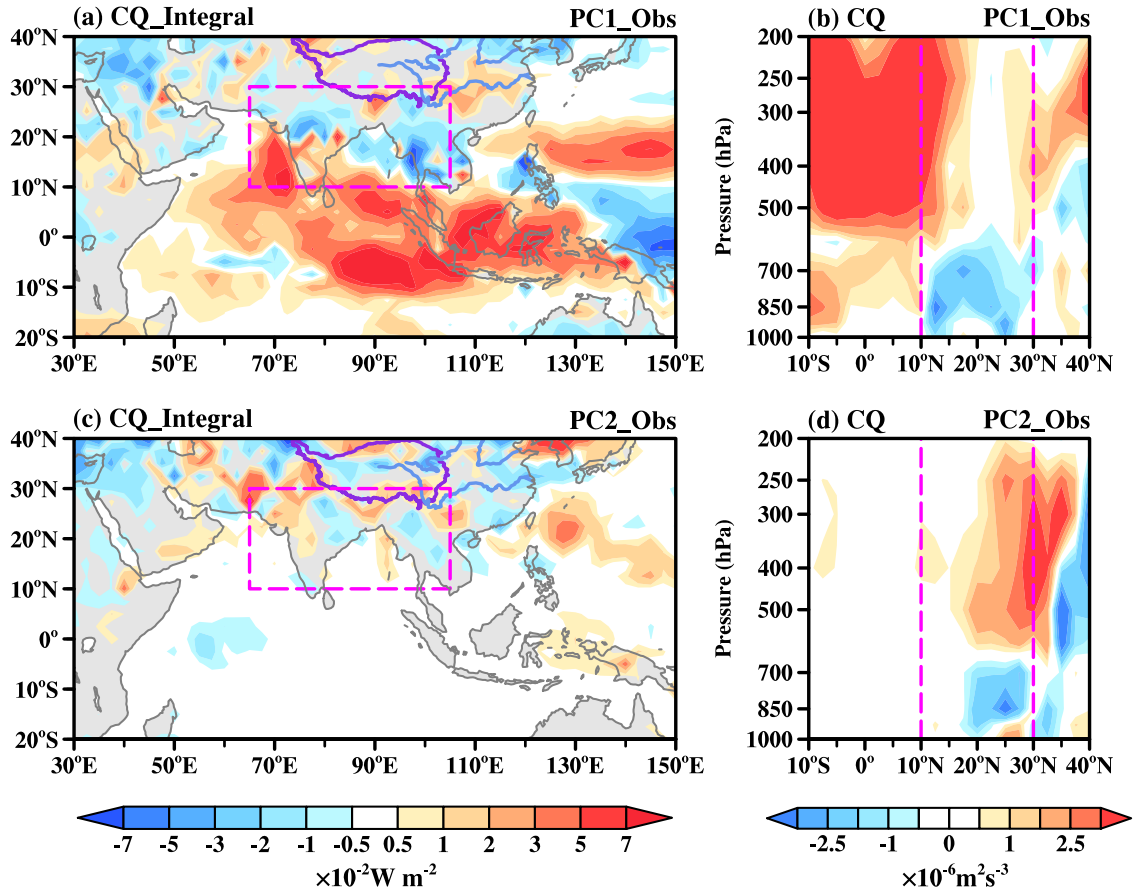


**Fig. 7 | Convective heating anomalies for the two leading SASM modes.** **a** Vertically integrated *CQ* in Eq. (5) from 1000 to 200 hPa (shading; $\times 10^{-2}$ W m$^{-2}$), calculated from perturbations ($u'$, $v'$, $\omega'$, $T'$) regressed onto PC1_Obs. **b** Vertical profiles of *CQ* zonally averaged over 65°–105°E (shading; $\times 10^{-6}$ m$^2$ s$^{-3}$) for PC1_Obs. **c**–**d** are the same as (**a**, **b**) but for PC2_Obs. The pink dashed box in (**a**) and (**c**) indicates the South Asian region (10°–30°N, 65°–105°E). The pink dashed lines in (**b**) and (**d**) indicate the latitudinal range of South Asia (10°–30°N).

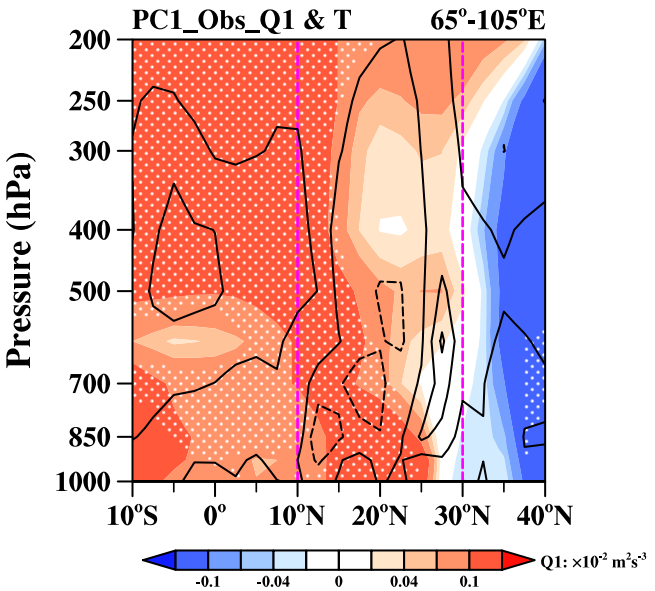


**Fig. 8 | Vertical structure of the thermal and diabatic heating anomalies for the first SASM mode.** Vertical profiles of anomalous temperature (shading; K) and $Q_1$ (contour; $\times 10^{-2}$ m$^2$s$^{-3}$) regressed onto PC1_Obs and zonally averaged over 65°–105°E. The pink dashed lines indicate the latitudinal range of South Asia (10°–30°N). Stippling areas indicate regression coefficients of temperature passing the 90% confidence level. The contour interval is $0.2 \times 10^{-2}$ m$^2$s$^{-3}$ (0, $\pm 0.2 \times 10^{-2}$, $\pm 0.4 \times 10^{-2}$, $\pm 0.6 \times 10^{-2}$).

which can be induced by the absence of Indo-Western Pacific Ocean Capacitor mode (IPOC) after removing the ENSO, with a weakening Kelvin wave response[55]. Compared to the first mode, the spatial pattern for the positive phase of the second SASM mode is less changed over South Asia after removing ENSO, except for the weakening of lower-level westerlies from the northern BOB to the Indo-China Peninsula. This change can be attributed to the weakening of the descending branch of the anomalous Walker circulation and the associated convection over the Maritime Continent after ENSO removal, which in turn reduces the induced Rossby wave response over South Asia[19,20].

After removing ENSO, the strongest climate mode on the interannual time scale, only the intensity of spatial patterns for the two SASM modes changes, while their primary features remain. Particularly, both leading SASM modes still exhibit zonally elongated circulation anomalies, which facilitate the EKE extraction from the background zonal confluent flow through *CK*. This suggests that internal atmospheric processes may play a significant role in shaping and regulating their structures[37].

To determine if the first two SASM modes are independent of external heat source at any specific location, we performed 132 independent experiments using the linear baroclinic model (LBM)[56], each forced by diabatic heating at different spatial locations within 55°N and 55°S based on the observed JJA basic state (hereafter EXP_LBM; see "Methods" and Supplementary Fig. S5)[46,57]. The resulting 132 cases of 850 hPa zonal and meridional wind responses are organized, according to the location of imposed diabatic heating, into two three-dimensional fields. The two leading modes of South Asian summer circulation are identified through MV-EOF analysis on the above two fields in 10°–30°N, 65°–105°E, accounting for 34 and 26% of the total variance. The spatial pattern for the

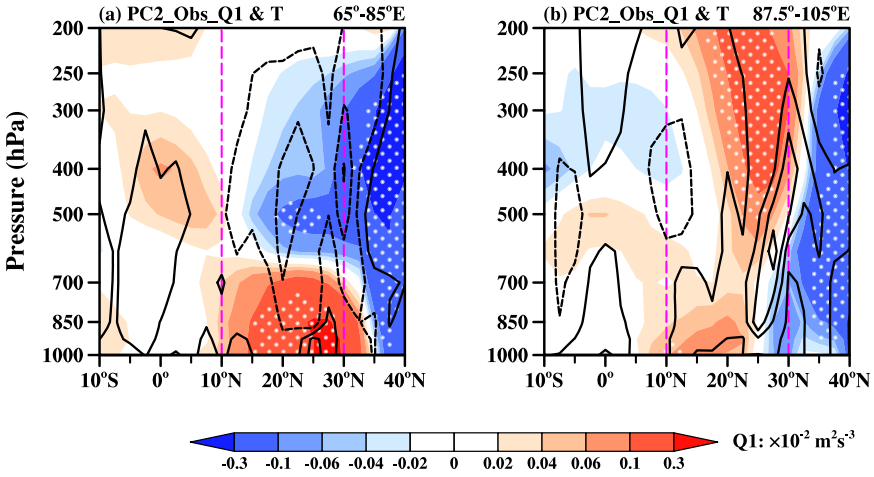


**Fig. 9 | Vertical structure of the thermal and diabatic heating anomalies for the second SASM mode.** Vertical profiles of anomalous temperature (shading; K) and $Q_1$ (contour; $\times 10^{-2}$ m$^2$ s$^{-3}$) regressed onto PC2_Obs and zonally averaged over (**a**) 65°–85°E and (**b**) 87.5°–105°E, respectively. The pink dashed lines indicate the latitudinal range of South Asia (10°–30°N). Stippling areas indicate regression coefficients of temperature passing the 90% confidence level. The contour interval is $0.2 \times 10^{-2}$ m$^2$ s$^{-3}$ (0, $\pm 0.2 \times 10^{-2}$, $\pm 0.4 \times 10^{-2}$, $\pm 0.6 \times 10^{-2}$).

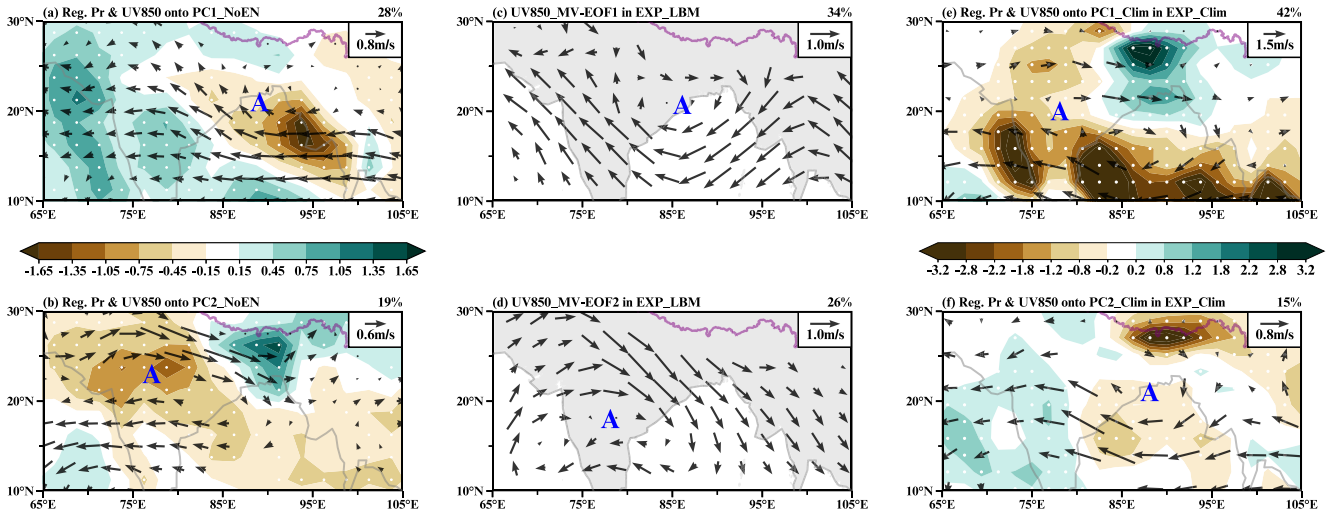


**Fig. 10 | Circulation characteristics of the two leading SASM modes independent of external forcings. a–b** are the same as Fig. 1, but for results removing the linear impact of ENSO. Spatial patterns of the (**c**) first and (**d**) second MV-EOF modes for the JJA 850 hPa winds among 132 diabatic forcing responses in the EXP_LBM (vectors; m s$^{-1}$). **e–f** are the same as Fig. 1, but for results from EXP_Clim. The letters A denote the centers of the anticyclonic anomalies. In (**a–b**) and (**e–f**), stippling areas indicate regression coefficients of precipitation passing the 90% confidence level. Only wind regression coefficients exceeding the 90% confidence level are shown.

positive phase of MV-EOF1 is characterized by a lower-level anomalous anticyclone over northern BOB, while that of MV-EOF2 features an anomalous anticyclone over central-northern India (Fig. 10c, d).

These circulation patterns from EXP_LBM are closely similar to those of two leading modes in observations correspondingly (Fig. 1). Since the imposed heat sources in the EXP_LBM are independent of one another, it denotes that the two observed SASM modes may be most readily excited regardless of any specific heat source. These findings indicate that, even though the two leading modes of SASM interannual variability can be regulated by external forcings, they may originate from internal atmospheric dynamics, supporting the preceding energy budget results.

To further confirm whether the two leading SASM modes can exist independently of external forcings, we perform a similar MV-EOF analysis of JJA precipitation and 850 hPa zonal wind from an atmosphere-only experiment (EXP_Clim) using the ECHAM version 5.4 atmospheric general circulation model (AGCM), driven by the monthly SST and sea ice climatology (see "Methods"). Figure 10e, f show the winds and rainfall associated with the first two leading modes in EXP_Clim, which together explain 57% of the total variance and pass the North's test. The positive phase of the first SASM mode in EXP_Clim resembles the second mode in observations (Fig. 1b), with stronger precipitation and circulation anomalies in South Asia. Similarly, the positive phase of the second SASM mode in EXP_Clim corresponds to the first mode in observations (Fig. 1a). The related negative precipitation anomalies over the WNP extend farther westward into the northern BOB, weakening the tripolar precipitation pattern. However, the associated circulation field remains highly comparable.

It is noteworthy that the order of two SASM modes in EXP_Clim is reversed compared to the results in observations (Figs. 1 and 10e, f). This is because the leading SASM modes in EXP_Clim are entirely driven by atmospheric internal processes. Despite the absence of external forcing, the SASM still exhibits significant interannual variability, with its dominant modes resembling those in observations. The analysis above suggests that the two leading SASM modes are likely atmospheric internal modes[35].

## Discussion

This study identifies two leading modes of SASM interannual variability and diagnoses their associated energy budget processes. The first mode is characterized by a northwest-southeast elongated tripolar precipitation pattern and a lower-level anomalous anticyclone over the northern BOB, while the second mode features negative precipitation anomalies and a lower-level anomalous anticyclone over central-northern India. The results

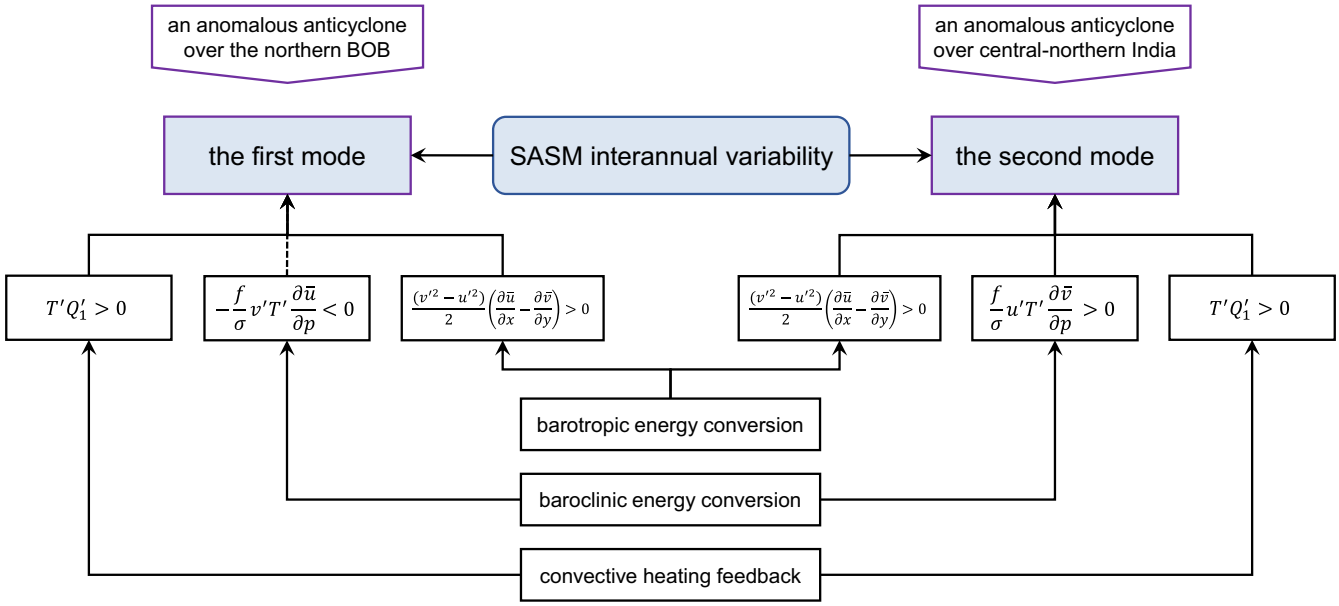


**Fig. 11** | Key energetic processes underlying the SASM interannual variability.

reveal that these SASM modes efficiently extract eddy energy from the mean state for their development and may originate from internal atmospheric dynamics.

The key energetic processes are summarized in a schematic diagram and explained as follows (Fig. 11). The barotropic energy conversion from the climatological zonal confluent flow to perturbations ($\frac{(v'^2-u'^2)}{2}\left(\frac{\partial \bar{u}}{\partial x}-\frac{\partial \bar{v}}{\partial y}\right) > 0$), representing the energy transfer from MKE to EKE, efficiently contributes to the maintenance of both the two leading SASM modes, characterized by zonally elongated circulation anomalies (Fig. 1). At 850 hPa, the background zonal confluent flow downstream of the Somali Jet and over the BOB-WNP helps to amplify the anomalous easterlies at 15°N and modulate the first SASM anomalies. Similarly, induced by the TP topography, the significantly subtropical westerly confluence over northeastern India can supply the anomalous anticyclone over central-northern India and help sustain the second SASM mode.

Different from barotropic energy conversion, baroclinic energy conversion, extracting EAPE from the mean thermal structure, exerts a damping effect on the first SASM mode while sustaining the second mode. Specifically, the northward eddy heat flux from offshore to inland over South Asia enhances the local meridional climatological temperature gradient at higher levels ($-\frac{f}{\sigma}v'T'\frac{\partial \bar{u}}{\partial p} < 0$), converting EAPE into MAPE and thereby damping the first mode. For the second mode, in contrast, the zonal eddy heat flux over northwestern India and southeastern TP can jointly weaken the zonal climatological temperature gradient correspondingly ($\frac{f}{\sigma}u'T'\frac{\partial \bar{v}}{\partial p} > 0$), efficiently generating EAPE through conversion from MAPE to maintain the second SASM anomalies. As the feedback to circulations, anomalous convective heating is also an effective source of EAPE, strengthening the two SASM modes ($T'Q_1' > 0$). The first mode exhibits prominently positive *CQ* over the eastern Arabian Sea and north of the BOB above 500 hPa, primarily associated with diabatic heating that intensifies warm temperature perturbations across South Asia. In contrast, the positive *CQ* for the second SASM mode is located over northwestern India and north of the BOB, due to the diabatic cooling (heating) that enhances cold (warm) perturbations over northwestern India (north of the BOB) at mid-to-upper levels.

The energy budget analysis highlights that the two SASM modes can extract eddy energy from the background mean state. Therefore, we further examine whether the two SASM modes can persist even in the absence of external forcings, namely SSTs and boundary conditions. After linearly removing ENSO, the critical external forcing on interannual scales, the major features of the two leading SASM modes remain (Fig. 10a, b). Circulation characteristics of the first two SASM modes identified in the EXP_LBM (Fig. 10c, d), an ensemble of steady atmospheric responses to diabatic heating at different spatial locations within 55°N and 55°S, are also similar to those in observations. It indicates these two modes may be most easily excited regardless of any specific heat source. Additionally, the dominant modes captured from EXP_Clim, driven by the climatological monthly SST and sea ice, resemble those in observations, even though the order in EXP_Clim is reversed due to strong internal variability (Fig. 10e, f). These results suggest that the two leading SASM modes may stem from internal atmospheric dynamics[35].

Both identified SASM modes are recurrent circulation patterns over South Asia and are indeed linked to recent climate extremes. For instance, circulation anomalies of the extreme rainfall event over the northeastern Indian subcontinent during the summer of 2020, the second wettest on record since 1901, closely resembles the positive phase of the first SASM mode[58]. Similarly, the extreme precipitation in the Indian monsoon region during the summer of 2022 is akin to the negative phase of the second SASM mode[10]. As revealed in this study, internal energetic processes contribute to the development of these SASM modes, which may help them to persist independently of external forcings. These findings provide new insights into the dynamics underlying SASM interannual variations and potentially contribute to addressing model biases in regional monsoon variability[59,60]. Unlike the PNA teleconnection, PJ pattern, and WNPAC[38,39,46,47], the SASM modes exhibit more complexity. Specifically, the significant monsoon–trade confluent center associated with the first mode is located in the WNP rather than South Asia[38], and the second mode, besides being dominated by local TP topography, may also be modulated by mid-to-high latitude baroclinic processes[4,61], which warrants further investigation. Moreover, whether these energy conversion processes contribute to addressing the uncertainty of SASM simulations in climate models also merits additional research.

## Methods

### Datasets used

The datasets used in this study include: (1) monthly SST with a 1.0° × 1.0° horizontal resolution provided by the Met Office Hadley Center Sea Ice and SST (HadISST) dataset[62]; (2) Monthly precipitation from the Climatic Research Unit gridded Time Series (CRU TS version 4.07) dataset[63], with a horizontal resolution of 0.5° × 0.5°; (3) Monthly global precipitation gridded at 2.5° × 2.5° horizontal resolution from the Global Precipitation Climatology Project (GPCP) dataset[64]; (4) Monthly atmospheric variables at multiple levels with a horizontal resolution of 2.5° × 2.5° from the fifth-

generation ECMWF reanalysis for the global climate and weather (ERA5)[65], including horizontal and vertical winds, geopotential height, and air temperature. All datasets cover the period from 1979 to 2022, and summer is defined as the average over June–August (JJA). To focus on the interannual timescale, the 9 year running mean of all variables has been removed. The results are consistent across the two precipitation datasets (figure not shown).

### MV-EOF analysis

Given the pronounced climatology and standard deviations of precipitation and 850 hPa zonal wind over South Asia (Supplementary Fig. S6), a MV-EOF analysis[41] is performed on these two variables over the region 10°–30°N, 65°–105°E to capture the major coupled features of atmospheric circulation and rainfall during the SASM in observations. The leading modes remain nearly unchanged when the 850 hPa meridional wind is additionally included (Supplementary Fig. S7). MV-EOF analysis is essentially an eigenvalue decomposition of a covariance matrix constructed from multiple variables. Before the analysis, each variable was normalized to ensure equal weighting regardless of its original units. The North's test was employed to analyze the significance of the MV-EOF mode[45].

### Energetic diagnostics

Energy diagnostic equations are utilized to evaluate the source and maintenance of SASM interannual variability[38,39,47,50,66]. The local barotropic energy conversion rate from the background mean flow to perturbations ($CK$), quantifying the energy transfer from MKE to EKE, is estimated based on the following formula:

$$CK = \underbrace{\frac{(v'^2 - u'^2)}{2}\left(\frac{\partial \bar{u}}{\partial x} - \frac{\partial \bar{v}}{\partial y}\right)}_{CK_x} \underbrace{-u'v'\left(\frac{\partial \bar{u}}{\partial y} + \frac{\partial \bar{v}}{\partial x}\right)}_{CK_y}. \quad (1)$$

Here, $u'$ and $v'$ represent the anomalous horizontal winds regressed onto PCs_Obs, while $\bar{u}$ and $\bar{v}$ denote those of climatology. $CK_x$ describes the energy conversion from the background confluent flow to perturbations, whereas $CK_y$ denotes the energy conversion from the mean horizontal wind shear to perturbations. Note that the confluence in this study denotes the directional convergence of the zonal or meridional wind components, different from total horizontal wind convergence. Positive $CK$ indicates the energy conversion from the background mean flow to anomalous atmospheric patterns, contributing to their development.

To measure the efficiency of $CK$ at 850-hPa in the maintenance of two SASM modes, we evaluate the time scale:

$$\tau_{CK} = \frac{\langle EKE \rangle}{\langle CK \rangle}, \quad (2)$$

where the brackets represent the area mean over South Asia (10°–30°N, 65°–105°E). The $\tau_{CK}$ denotes how long it takes for the local EKE associated with anomalous patterns ($EKE = \frac{(u'^2+v'^2)}{2}$) to be fully replenished through $CK$.

The local baroclinic energy conversion rate from the MAPE to EAPE ($CP$) is diagnosed based on the following equation:

$$CP = \left[\underbrace{\frac{f}{\sigma}u'T'\frac{\partial \bar{v}}{\partial p}}_{CP_x} \underbrace{-\frac{f}{\sigma}v'T'\frac{\partial \bar{u}}{\partial p}}_{CP_y}\right], \quad (3)$$

where $u'$, $v'$, $\bar{u}$, and $\bar{v}$ are similar to those in Eq. (1); $T'$ and $p$ are the anomalous temperature regressed onto PCs_Obs and atmospheric pressure, respectively; the square bracket represents the vertical integral taken from the surface through 200 hPa; $\sigma = \left(\frac{R\bar{T}}{C_p p}\right) - \left(\frac{\partial \bar{T}}{\partial p}\right)$ denotes the static stability, which is consistently positive at 500 hPa in JJA (Supplementary Fig. S8) and suggest the sign of $CP$ is primarily determined by the eddy heat flux ($u'T'$ and $v'T'$) and background state $\left(\frac{\partial \bar{v}}{\partial p}\right.$ and $\left.\frac{\partial \bar{u}}{\partial p}\right)$; $f$, $R$, and $C_p$ are the Coriolis parameter, gas constant (287 J K$^{-1}$kg$^{-1}$), and specific heat at constant pressure (1,004 J K$^{-1}$kg$^{-1}$), respectively. Positive $CP$ indicates the energy conversion from the climatological thermal structure toward anomalous atmospheric patterns, converting MAPE into EAPE. $CP_x$ and $CP_y$ denote the zonal and meridional components of $CP$, respectively. Similar to barotropic energy conversion, we estimate the time scale of effective $CP$ for maintaining the atmospheric modes:

$$\tau_{CP} = \frac{\langle [EAPE] \rangle}{\langle CP \rangle}. \quad (4)$$

Here, $[EAPE] = \left[\frac{RT'^2}{2\sigma p}\right]$ denotes the vertically integrated EAPE associated with anomalous patterns, and $\tau_{CP}$ measures the efficiency of $CP$ in supplying local EAPE to perturbations.

Considering the strong convective feedback in tropical South Asia[67], the generation of EAPE induced by anomalous convective heating rate ($CQ$) is assessed as

$$CQ = \frac{R}{C_p}\left[\frac{T'Q_1'}{p\sigma}\right], \quad (5)$$

where $Q_1'$ denotes the anomalous atmospheric apparent heat source[52,68]. $Q_1'$ can be calculated from:

$$Q_1' = C_p\frac{\partial T'}{\partial t} - C_p\left(\omega'\sigma - V_h' \cdot \nabla_h \bar{T}\right). \quad (6)$$

Here, $V_h'$ and $\omega'$ represent the anomalous horizontal velocity vector and anomalous vertical velocity regressed onto PCs_Obs, respectively; $\bar{T}$ and $t$ are the climatological temperature and time. Positive $CQ$ indicates the generation of EAPE by diabatic heating (cooling) intensifies warm (cold) temperature perturbations. The efficiency of $CQ$ in replenishing the local EAPE for anomalous patterns is quantified as

$$\tau_{CQ} = \frac{\langle [EAPE] \rangle}{\langle CQ \rangle}. \quad (7)$$

It is noted that the perturbed anomaly terms contributing to $CK$, namely $u'^2$, $v'^2$, and $u'v'$; those governing $CP$, including $u'T'$ and $v'T'$; and those determining $CQ$, namely $T'Q_1'$, remain unchanged if the phase of the MV-EOF mode is reversed. Therefore, the energy diagnostic results based on the positive phase of the SASM modes in this study are equally applicable to their negative phase. It indicates these energy conversion processes are phase-independent.

### Removing ENSO linear effects

To represent ENSO in winter, the Niño-3.4 index is defined by the averaged SST anomalies in December-February (DJF) within 5°S–5°N and 120°–170°W. The process of excluding ENSO's linear impact on SASM interannual variability involves three steps[53,54,69]. First, to track the influence of the preceding ENSO in the subsequent summer, a tropical SST index ($I_{EN}$) is defined as the JJA areal mean SSTs in the tropics, weighted by SST regression coefficients in each grid relative to the preceding DJF Niño3.4 index (passing the 95% confidence level). Then, ENSO's impact is linearly removed through the following equation:

$$X_{NoEN} = X - I_{EN} \times Reg\left[X\ onto\ I_{EN}\right]. \quad (8)$$

Here, $X$ represents original variable fields, $I_{EN} \times Reg\left[X\ onto\ I_{EN}\right]$ denotes reconstruction fields with ENSO's impact, and $X_{NoEN}$ indicates variable fields independent of $I_{EN}$. Lastly, two leading SASM modes without

the influence of ENSO are captured by applying a similar MV-EOF analysis to $X_{NoEN}$.

### LBM experiments

A LBM[56] is employed to simulate 132 independent steady responses to diabatic heating at different spatial locations, based on the primitive equations linearized at the observed JJA basic state (EXP_LBM). The dry version of LBM, run at a horizontal resolution of T42 with 20 sigma levels, has been widely utilized to analyze individual responses to regional heat sources[20,70,71]. We divide the domain within 55°N and 55°S into 132 subregions, each with a size of 10° latitude × 30° longitude. In each subregion, an idealized heat source with a peak of 1 K day$^{-1}$ at the 0.45 sigma level is independently implemented using the LBM[16,72] (Supplementary Fig. S5). The experiments are integrated for 50 days, with the averages from 40 to 50 days representing the steady states. The resulting 132 cases of steady responses are further organized, according to the location of imposed forcings, into three-dimensional fields (dimensions: [cases, latitudes, longitudes]).

### Climatological SST and sea ice AGCM experiment

To study atmospheric internal variability, an atmosphere-only simulation from the ECHAM version 5.4 AGCM developed by the Max Planck Institute for Meteorology is utilized[73]. The model has a triangular truncation at zonal wavenumber 63 (T63; approximately 1.9° × 1.9°) and 19 vertical levels, which is forced by the climatological monthly SST and sea ice (EXP_Clim). The experiment is integrated for 100 years, with the final 50 years utilized for analysis. Due to the absence of SST variability beyond the monthly time scale, the interannual variation primarily results from atmospheric internal processes[74].

## Data availability

The datasets are available in a public repository. The monthly SST data from HadISST are available at https://www.metoffice.gov.uk/hadobs/hadisst/. The monthly land precipitation from the CRU TS v.4.07 dataset is provided at https://crudata.uea.ac.uk/cru/data/hrg/. The monthly global precipitation data are obtained by GPCP at https://psl.noaa.gov/data/gridded/data.gpcp.html. The monthly atmospheric reanalysis data from the ERA5 are openly obtained at https://cds.climate.copernicus.eu/datasets/reanalysis-era5-pressure-levels-monthly-means?tab=overview.

## Code availability

The data in this study are analyzed with Python and NCAR Command Language (NCL). The relevant codes used in this work are available upon reasonable request from the first author, Tong Lu (lutong211@mails.ucas.ac.cn).

Received: 31 March 2025; Accepted: 18 June 2025;
Published online: 13 August 2025

## References

1. Gadgil, S. & Gadgil, S. The Indian monsoon, GDP and agriculture. *Econ. Political Wkly.* **41**, 4887–4895 (2006).
2. Turner, A. G. & Annamalai, H. Climate change and the South Asian summer monsoon. *Nat. Clim. Change* **2**, 587–595 (2012).
3. He, L., Zhou, T. & Guo, Z. Past warm intervals inform the future South Asian summer monsoon. *Nature* **641**, 653–659 (2025).
4. Ding, Q. & Wang, B. Circumglobal teleconnection in the Northern Hemisphere summer. *J. Clim.* **18**, 3483–3505 (2005).
5. Wu, R. Relationship between Indian and East Asian summer rainfall variations. *Adv. Atmos. Sci.* **34**, 4–15 (2017).
6. Liu, Y. & Huang, R. Linkages between the South and East Asian monsoon water vapor transport during boreal summer. *J. Clim.* **32**, 4509–4524 (2019).
7. Kosaka, Y. Coupling of the Indian, western North Pacific, and East Asian summer monsoons. In *Indian Summer Monsoon Variability* 263–286 (Elsevier, 2021).
8. Yang, X., Huang, P., Liu, Y. & Chen, D. An interdecadal enhancement of the impact of ENSO on the summer Northeast Asian circulation around 1999/2000 through the Silk Road Pattern. *J. Clim.* **35**, 7481–7497 (2022).
9. Tang, S. et al. Linkages of unprecedented 2022 Yangtze River Valley heatwaves to Pakistan flood and triple-dip La Niña. *NPJ Clim. Atmos. Sci.* **6**, 44 (2023).
10. Song, Q., Wang, C., Yao, Y. & Fan, H. Unraveling the Indian monsoon's role in fueling the unprecedented 2022 marine heatwave in the western North Pacific. *NPJ Clim. Atmos. Sci.* **7**, 90 (2024).
11. Zhu, J. & Wu, Z. Indian summer monsoon's role in shaping variability in Arctic sea ice. *NPJ Clim. Atmos. Sci.* **7**, 1–15 (2024).
12. Yu, H., Zhou, T. & He, L. Indian summer monsoon precipitation dominates the reproduction of circumglobal teleconnection pattern: a comparison of CMIP5 and CMIP6 models. *J. Clim.* **37**, 5009–5023 (2024).
13. Mishra, V., Smoliak, B. V., Lettenmaier, D. P. & Wallace, J. M. A prominent pattern of year-to-year variability in Indian Summer monsoon rainfall. *Proc. Natl. Acad. Sci. USA* **109**, 7213–7217 (2012).
14. Zhou, Z., Xie, S. & Zhang, R. Variability and predictability of Indian rainfall during the monsoon onset month of June. *Geophys. Res. Lett.* **46**, 14782–14788 (2019).
15. Zhang, T., Jiang, X., Yang, S., Chen, J. & Li, Z. A predictable prospect of the South Asian summer monsoon. *Nat. Commun.* **13**, 7080 (2022).
16. Lu, T., Hu, K., Huang, G. & Wang, Y. Optimal atmospheric heat sources for the interannual variability of South Asian summer monsoon. *Geophys. Res. Lett.* **51**, e2024GL112059 (2024).
17. Chowdary, J. S. et al. Indian summer monsoon rainfall variability in response to differences in the decay phase of El Niño. *Clim. Dyn.* **48**, 2707–2727 (2017).
18. Chowdary, J. S., Patekar, D., Srinivas, G., Gnanaseelan, C. & Parekh, A. Impact of the Indo-Western Pacific Ocean Capacitor mode on South Asian summer monsoon rainfall. *Clim. Dyn.* **53**, 2327–2338 (2019).
19. Wang, B., Li, J. & He, Q. Variable and robust East Asian monsoon rainfall response to El Niño over the past 60 years (1957–2016). *Adv. Atmos. Sci.* **34**, 1235–1248 (2017).
20. Hu, P. et al. Revisiting the linkage between the Pacific–Japan pattern and Indian summer monsoon rainfall: the crucial role of the maritime continent. *Geophys. Res. Lett.* **51**, e2023GL106982 (2024).
21. Ashok, K., Guan, Z. & Yamagata, T. Impact of the Indian Ocean dipole on the relationship between the Indian monsoon rainfall and ENSO. *Geophys. Res. Lett.* **28**, 4499–4502 (2001).
22. Chung, C. E. & Ramanathan, V. Weakening of North Indian SST gradients and the monsoon rainfall in India and the Sahel. *J. Clim.* **19**, 2036–2045 (2006).
23. Rao, S. A., Chaudhari, H. S., Pokhrel, S. & Goswami, B. N. Unusual central Indian drought of summer monsoon 2008: role of southern tropical Indian Ocean warming. *J. Clim.* **23**, 5163–5174 (2010).
24. Sabeerali, C. T., Ajayamohan, R. S., Bangalath, H. K. & Chen, N. Atlantic zonal mode: an emerging source of Indian summer monsoon variability in a warming world. *Geophys. Res. Lett.* **46**, 4460–4467 (2019).
25. Rajeevan, M. & Sridhar, L. Inter-annual relationship between Atlantic sea surface temperature anomalies and Indian summer monsoon. *Geophys. Res. Lett.* **35**, 2008GL036025 (2008).
26. Wu, G. et al. Tibetan Plateau climate dynamics: recent research progress and outlook. *Natl Sci. Rev.* **2**, 100–116 (2015).
27. He, H., McGinnis, J. W., Song, Z. & Yanai, M. Onset of the Asian summer monsoon in 1979 and the effect of the Tibetan Plateau. *Mon. Weather Rev.* **115**, 1966–1995 (1987).
28. Wu, G. & Zhang, Y. Tibetan Plateau forcing and the timing of the monsoon onset over South Asia and the South China Sea. *Mon. Weather Rev.* **126**, 913–927 (1998).
29. Kasahara, A. & Washington, W. M. General circulation experiments with a six-layer NCAR model, including orography, cloudiness and surface temperature calculations. *J. Atmos. Sci.* **28**, 657–701 (1971).

30. Hahn, D. G. & Manabe, S. The role of mountains in the South Asian monsoon circulation. *J. Atmos. Sci.* **32**, 1515–1541 (1975).
31. Barnett, T. P., Dümenil, L., Schlese, U. & Roeckner, E. The effect of Eurasian snow cover on global climate. *Science* **239**, 504–507 (1988).
32. Bamzai, A. S. & Shukla, J. Relation between Eurasian snow cover, snow depth, and the Indian summer monsoon: an observational study. *J. Clim.* **12**, 3117–3132 (1999).
33. Zhang, T. et al. The weakening relationship between Eurasian spring snow cover and Indian summer monsoon rainfall. *Sci. Adv.* **5**, eaau8932 (2019).
34. Latif, M., Biercamp, J., Storch, Hvon, McPhaden, M. J. & Kirk, E. Simulation of ENSO related surface wind anomalies with an atmospheric GCM forced by observed SST. *J. Clim.* **3**, 509–521 (1990).
35. Goswami, B. N. Interannual variations of Indian summer monsoon in a GCM: external conditions versus internal feedbacks. *J. Clim.* **11**, 501–522 (1998).
36. Goswami, B. N. & Xavier, P. K. Dynamics of "internal" interannual variability of the Indian summer monsoon in a GCM. *J. Geophys. Res. Atmos*. **110** https://doi.org/10.1029/2005JD006042 (2005).
37. Hsu, P. & Yang, Y. Contribution of atmospheric internal processes to the interannual variability of the South Asian summer monsoon. *Int. J. Climatol.* **36**, 2917–2930 (2016).
38. Hu, K., Huang, G., Xie, S.-P. & Long, S.-M. Effect of the mean flow on the anomalous anticyclone over the Indo-Northwest Pacific in post-El Niño summers. *Clim. Dyn.* **53**, 5725–5741 (2019).
39. Kosaka, Y. & Nakamura, H. Structure and dynamics of the summertime Pacific–Japan teleconnection pattern. *Q. J. R. Meteorol. Soc.* **132**, 2009–2030 (2006).
40. Lu, M. & Ren, H.-L. Linkage between Southeast and South Asian summer monsoons: relative roles of the Pacific-Japan pattern and the El Niño-Southern Oscillation. *J. Clim.* **38**, 1421–1433 (2025).
41. Wang, B. The vertical structure and development of the ENSO anomaly mode during 1979–1989. *J. Atmos. Sci.* **49**, 698–712 (1992).
42. Xiang, B. & Wang, B. Mechanisms for the advanced Asian summer monsoon onset since the mid-to-late 1990s. *J. Clim.* **26**, 1993–2009 (2013).
43. Bombardi, R. J., Moron, V. & Goodnight, J. S. Detection, variability, and predictability of monsoon onset and withdrawal dates: a review. *Int. J. Climatol.* **40**, 641–667 (2020).
44. Hu, P. et al. The leading mode and factors for coherent variations among the subsystems of tropical Asian summer monsoon onset. *J. Clim.* **35**, 1597–1612 (2022).
45. North, G. R., Bell, T. L., Cahalan, R. F. & Moeng, F. J. Sampling errors in the estimation of empirical orthogonal functions. *Mon. Weather Rev.* **110**, 699–706 (1982).
46. Simmons, A. J., Wallace, J. M. & Branstator, G. W. Barotropic wave propagation and instability, and atmospheric teleconnection patterns. *J. Atmos. Sci.* **40**, 1363–1392 (1983).
47. Tang, H., Hu, K., Huang, G., Wang, Y. & Tao, W. Intensification and northward extension of Northwest Pacific anomalous anticyclone in El Niño decaying mid-summer: an energetic perspective. *Clim. Dyn.* **58**, 591–606 (2022).
48. Jain, S., Mishra, S. K., Anand, A., Salunke, P. & Fasullo, J. T. Historical and projected low-frequency variability in the Somali Jet and Indian summer monsoon. *Clim. Dyn.* **56**, 749–765 (2021).
49. Upadhyaya, P., Mishra, S. K., Fasullo, J. T. & Kang, I.-S. Attributing the recent weakening of the South Asian subtropical westerlies. *NPJ Clim. Atmos. Sci.* **7**, 283 (2024).
50. Wang, Y. et al. Asymmetric impacts of El Niño and La Niña on the Pacific–South America teleconnection pattern. *J. Clim.* **35**, 1825–1838 (2022).
51. Watanabe, M. Linear Baroclinic Model (LBM) Package Users' Guide. Center for Climate System Research https://ccsr.aori.u-tokyo.ac.jp/~lbm/lbm/doc2.2.pdf (University of Tokyo, 2005).
52. Lau, K.-H. & Lau, N.-C. The energetics and propagation dynamics of tropical summertime synoptic-scale disturbances. *Mon. Weather Rev.* **120**, 2523–2539 (1992).
53. Lu, T., Zhu, Z., Yang, Y., Ma, J. & Huang, G. Formation mechanism of the ENSO-independent summer western North Pacific anomalous anticyclone. *J. Clim.* **36**, 1711–1726 (2023).
54. Yang, Y., Zhu, Z., Shen, X., Jiang, L. & Li, T. The influences of Atlantic sea surface temperature anomalies on the ENSO-independent interannual variability of East Asian summer monsoon rainfall. *J. Clim.* **36**, 677–692 (2023).
55. Xie, S.-P. et al. Indo-western Pacific ocean capacitor and coherent climate anomalies in post-ENSO summer: a review. *Adv. Atmos. Sci.* **33**, 411–432 (2016).
56. Watanabe, M. & Kimoto, M. Atmosphere-ocean thermal coupling in the North Atlantic: a positive feedback. *Q. J. R. Meteorol. Soc.* **126**, 3343–3369 (2000).
57. Branstator, G. Analysis of general circulation model sea-surface temperature anomaly simulations using a linear model. Part I: Forced solutions. *J. Atmos. Sci.* **42**, 2225–2241 (1985).
58. Tang, H. et al. Increasing 2020-like boreal summer rainfall extremes over Northeast Indian subcontinent under greenhouse warming. *Geophys. Res. Lett.* **49**, e2021GL096377 (2022).
59. Zhou, S., Huang, P., Huang, G. & Hu, K. Leading source and constraint on the systematic spread of the changes in East Asian and western North Pacific summer monsoon. *Environ. Res. Lett.* **14**, 124059 (2019).
60. Wang, Y. et al. Understanding the eastward shift and intensification of the ENSO teleconnection over South Pacific and Antarctica under greenhouse warming. *Front. Earth Sci.* **10**, 916624 (2022).
61. Krishnan, R., Kumar, V., Sugi, M. & Yoshimura, J. Internal feedbacks from monsoon—midlatitude interactions during droughts in the Indian summer monsoon. *J. Atmos. Sci.* **66**, 553–578 (2009).
62. Rayner, N. A. et al. Global analyses of sea surface temperature, sea ice, and night marine air temperature since the late nineteenth century. *J. Geophys. Res. Atmos*. **108** https://doi.org/10.1029/2002JD002670 (2003).
63. Harris, I., Osborn, T. J., Jones, P. & Lister, D. Version 4 of the CRU TS monthly high-resolution gridded multivariate climate dataset. *Sci. Data* **7**, 109 (2020).
64. Adler, R. F. et al. The version-2 Global Precipitation Climatology Project (GPCP) monthly precipitation analysis (1979–present). *J. Hydrometeorol.* **4**, 1147–1167 (2003).
65. Hersbach, H. et al. ERA5 monthly averaged data on pressure levels from 1940 to present. *Copernicus Climate Change Service (C3S) Climate Data Store (CDS)* https://doi.org/10.24381/cds.6860a573 (2023).
66. Wang, Y., Hu, K., Huang, G. & Tao, W. The role of nonlinear energy advection in forming asymmetric structure of ENSO teleconnections over the North Pacific and North America. *Geophys. Res. Lett.* **50**, e2023GL105277 (2023).
67. Wang, B. & Fan, Z. Choice of South Asian summer monsoon indices. *Bull. Am. Meteorol. Soc.* **80**, 629–638 (1999).
68. Yanai, M., Esbensen, S. & Chu, J.-H. Determination of bulk properties of tropical cloud clusters from large-scale heat and moisture budgets. *J. Atmos. Sci.* **30**, 611–627 (1973).
69. Gong, D.-Y. et al. Spring Arctic Oscillation-East Asian summer monsoon connection through circulation changes over the western North Pacific. *Clim. Dyn.* **37**, 2199–2216 (2011).
70. Lu, R. & Lin, Z. Role of subtropical precipitation anomalies in maintaining the summertime meridional teleconnection over the western North Pacific and East Asia. *J. Clim.* **22**, 2058–2072 (2009).
71. Sampe, T. & Xie, S.-P. Large-scale dynamics of the Meiyu-Baiu rainband: environmental forcing by the westerly Jet. *J. Clim.* **23**, 113–134 (2010).
72. Hu, K. & Long, S.-M. Optimal heat source for the interannual variability of the western North Pacific summer monsoon. *Atmos. Ocean. Sci. Lett.* **13**, 41–47 (2020).

73. Roeckner, E. et al. The atmospheric general circulation model ECHAM5. Part I: Model description. Technical Report 349 (Max Planck Institute for Meteorology, 2003).
74. Zhou, Z.-Q., Xie, S.-P., Zhang, G. J. & Zhou, W. Evaluating AMIP skill in simulating interannual variability over the Indo–Western Pacific. *J. Clim.* **31**, 2253–2265 (2018).

## Acknowledgments

This work was supported by the National Natural Science Foundation of China (Grants 42141019, 42175040, 42261144687, 42475046) and the Youth Innovation Promotion Association of CAS (2021072). T.L. thanks the financial support from the China Scholarship Council (202404910419). The authors would like to thank the editor and three anonymous reviewers for their comments and suggestions that have helped us improve the final manuscript.

## Author contributions

T.L. and K.H. designed the study, executed data analyses, and authored the original draft. All authors contributed to the critical discussion, review, and improvement of this paper.

## Competing interests

The authors declare no competing interests.

## Additional information

**Supplementary information** The online version contains supplementary material available at https://doi.org/10.1038/s41612-025-01143-4.

**Correspondence** and requests for materials should be addressed to Kaiming Hu or Gang Huang.